nature nanotechnology

ARTICLES

https://doi.org/10.1038/s41565-021-01052-6

Reversible strain-induced magnetic phase transition in a van der Waals magnet

John Cenker[1], Shivesh Sivakumar[2], Kaichen Xie[2], Aaron Miller[1], Pearl Thijssen[1], Zhaoyu Liu[1], Avalon Dismukes[3], Jordan Fonseca[1], Eric Anderson[1], Xiaoyang Zhu[3], Xavier Roy[3], Di Xiao[1,2], Jiun-Haw Chu[1], Ting Cao[2]✉ and Xiaodong Xu[1,2]✉

Mechanical deformation of a crystal can have a profound effect on its physical properties. Notably, even small modifications of bond geometry can completely change the size and sign of magnetic exchange interactions and thus the magnetic ground state. Here we report the strain tuning of the magnetic properties of the A-type layered antiferromagnetic semiconductor CrSBr achieved by designing a strain device that can apply continuous, in situ uniaxial tensile strain to two-dimensional materials, reaching several percent at cryogenic temperatures. Using this apparatus, we realize a reversible strain-induced antiferromagnetic-to-ferromagnetic phase transition at zero magnetic field and strain control of the out-of-plane spin-canting process. First-principles calculations reveal that the tuning of the in-plane lattice constant strongly modifies the interlayer magnetic exchange interaction, which changes sign at the critical strain. Our work creates new opportunities for harnessing the strain control of magnetism and other electronic states in low-dimensional materials and heterostructures.

Controllable transitions between different phases of matter with distinct symmetries are at the heart of condensed matter physics and play important roles in modern nanotechnology. For instance, switching the sign of spin–spin exchange interactions in materials with magnetic order can lead to transitions between antiferromagnetic (AFM) and ferromagnetic (FM) phases that enable new types of magnetoresistive device[1–4]. The recent discovery of atomically thin van der Waals (vdW) magnets provides a new platform for the manipulation of magnetic properties with versatile methods of control, including electrical and nanomechanical means[5,6]. For the latter, hydrostatic pressure has been used to switch AFM to FM states in the A-type antiferromagnet CrI_3 at zero magnetic field[7,8]. However, the pressure-induced magnetic state switching in CrI_3 is non-reversible, as it originates from the rearrangement of layer stacking from monoclinic to rhombohedral. In addition, only discrete hydrostatic pressures can be applied due to the limitation of pressure cells. It would thus be highly desirable to develop a continuously tunable knob as well as discover a suitable material system for achieving reversible magnetic phase transitions.

Tensile strain is a proven method for tuning the fundamental properties of three-dimensional bulk quantum materials. Examples include the strain control of superconducting[9,10], nematic[11] and topological phases[12] by the direct modification of lattice constant and symmetry of a given crystal. Several previous studies have also demonstrated the switching of magnetic phases by ex situ strain techniques, such as thin-film epitaxy[13], pressure[14] and stretching of a polymer layer[15]. For vdW magnets, several recent works have highlighted the tantalizing opportunities for the strain control of magnetic properties such as ordering temperature[16,17], coercive fields[17] and Néel vectors[18] in several systems, with predicted magnetic phase transitions in certain materials under a large strain[19–22]. However, the experimental realization of a reversible AFM-to-FM phase transition by continuous strain tuning in either bulk or two-dimensional (2D) crystals remains a challenge. One difficulty lies in the lack of cryo-strain devices that can apply large (over 1%) and in situ tunable strain.

In this work, we design a cryo-strain device capable of applying large strains to 2D materials. This new capability enables the continuous and reversible tuning of the magnetic properties of a recently discovered vdW magnet CrSBr, including magnetic anisotropy, interlayer exchange interaction and magnetic ground state. Our cryogenic strain apparatus is based on a piezoelectric strain cell (Fig. 1a and Extended Data Fig. 1), which has previously been used to apply uniaxial strain to bulk crystals[10,12,23]. To apply large strain on thin vdW flakes, we cleave a silicon substrate to produce a microscopic gap over which it is possible to suspend a sample (Fig. 1b and Methods). Since the applied strain is equal to the fractional change in length, the small gap can, in principle, apply very large strain to the sample, given the sample does not yield or slide.

Determination of strain through Raman spectroscopy

CrSBr is an A-type AFM semiconductor with an in-plane easy axis along *b* (Fig. 1b)[22,24–26]. Due to the anisotropic crystal structure, exfoliated thin CrSBr flakes typically exhibit a rectangular structure with a long edge of over 100 μm along the *a* axis and a short edge of ~10 μm along the *b* axis. This aspect ratio is ideal for suspending the sample with the gap perpendicular to the *a* axis (Fig. 1b). To estimate the applied strain on CrSBr, we compare the Raman spectra taken on the strained region with the spectrum on an unstrained area far from the gap (Fig. 1c). To this end, we have calibrated the strain shift rate of the phonon mode at ~345 cm^{-1} (labelled as P_3) versus the piezo voltage using a strain gauge heterostructure (Extended Data Fig. 2). The calibration yields a redshift rate of ~4.2 cm^{-1} $\%^{-1}$, in good agreement with the redshift rate of ~4.4 cm^{-1} $\%^{-1}$ predicted by first-principles calculations. Figure 1d shows the Raman intensity plot of a suspended sample as a function of the applied piezo voltage. The response of P_3 is highly linear, indicating negligible sample slippage. We note that P_3 is broadened at a low piezo

[1]Department of Physics, University of Washington, Seattle, WA, USA. [2]Department of Materials Science and Engineering, University of Washington, Seattle, WA, USA. [3]Department of Chemistry, Columbia University, New York, NY, USA. ✉e-mail: tingcao@uw.edu; xuxd@uw.edu

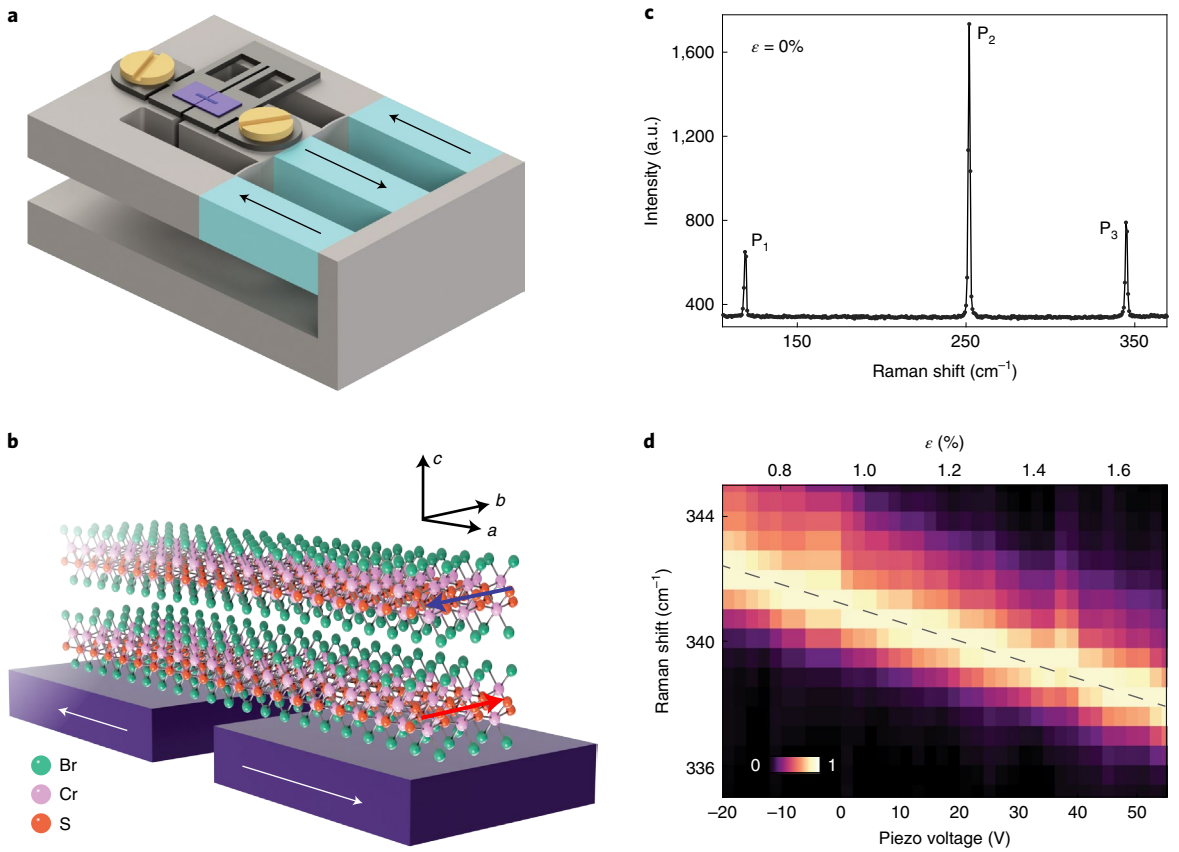

Fig. 1 | Cryo-strain device and strain tuning of a Raman mode. a, Schematic of the strain cell based on three parallel piezo stacks glued to a titanium backing and flexure. The strain is applied to vdW materials placed on a gapped SiO_2/Si substrate that is fixed on top of the strain device (Methods). **b**, Schematic of the CrSBr sample suspended over a micrometre-scale gap in the SiO_2/Si substrate. The strain is aligned with the crystal (*a*) axis of the CrSBr, which is orthogonal to the easy (*b*) axis. The red and blue arrows on the CrSBr depict the AFM interlayer coupling that produces an A-type layered AFM structure. **c**, Raman spectrum of a free-standing thin CrSBr flake. **d**, P_3 Raman mode as a function of piezo voltage of a suspended thin CrSBr flake. The strain values are determined using the measured CrSBr Raman shift rate (Extended Data Fig. 2) and the unstrained spectrum in **c**.

voltage due to strain gradients near the edge of the gap. As the gap is opened, the strain becomes more homogeneous as evidenced by the sharper peak at a high piezo voltage. Using the determined shift rate of 4.2 cm^{-1} $\%^{-1}$ and a zero-strain peak energy of 345 cm^{-1} taken far off the gap (Fig. 1c), the applied strain is determined to range from ~0.6% up to 1.7%. This range of applied strain is typical for the samples we measured and is substantially higher than previous cryo-strain experiments that rely on bendable substrates[17,27].

Strain-induced magnetic phase transition

After strain calibration, we proceed to demonstrate control of magnetism in CrSBr with high strains. Since CrSBr has an in-plane magnetic easy axis, polar reflective magnetic circular dichroism (RMCD) is a poor probe of the in-plane magnetic ground states. A recent study[24] revealed rich excitonic features in both photoluminescence (PL) and optical absorption spectra of CrSBr. Although not all the spectral features are well understood, the work established that the excitons in thin CrSBr flakes are sensitive to the interlayer magnetic order and redshift at the AFM-to-FM phase transition. This enables us to probe the interlayer magnetic coupling through the exciton PL spectrum. The data presented in the rest of this paper were taken from an ~20 nm CrSBr flake (Extended Data Fig. 3 provides additional sample details).

Figure 2a shows the PL intensity plot as a function of the applied strain and photon energy in the absence of a magnetic field. Several discrete exciton PL features are observed, at similar energies to the ones reported in ref. [24]. These peaks remain nearly unchanged as the strain increases from 0.7% to about 1.1%. This observation agrees with the first-principles calculations that suggest that a tensile strain of <1% only results in a continuous change of <5 meV of the band-gap in the AFM phase (Extended Data Fig. 4a). Remarkably, as the strain increases further, the intensity of these peaks decreases, and a new set of peaks emerge. Above ~1.3%, the new features dominate the spectrum, which does not show any appreciable change as the strain increases further. Figure 2b plots the PL spectra at two selected strains, namely, 0.9% (black) and 1.4% (blue), which correspond to before and after the abrupt, strain-induced changes to the PL, respectively. The spectra reveal a clear ~12 meV redshift between the low- and high-strain states, whereas the number of peaks does not change, that is, the PL pattern remains the same. We measured several samples and observed similar jumps in the PL spectrum (Extended Data Fig. 5).

To determine the origin of the PL shift, we compare the strain-dependent PL spectra with the unstrained spectra of different magnetic states. The black curve in Fig. 2c corresponds to the PL spectrum of the A-type AFM ground state of unstrained CrSBr at zero magnetic field. The bottom inset illustrates the spin configuration. Each monolayer has an FM intralayer coupling with spins aligned along the magnetic easy axis (*b* axis), whereas the interlayer coupling is AFM. The blue spectrum is the PL of CrSBr with a magnetic field of 0.4 T applied along the easy axis. Since the applied magnetic field is larger than the coercive field of about 0.22 T (Fig. 2c,

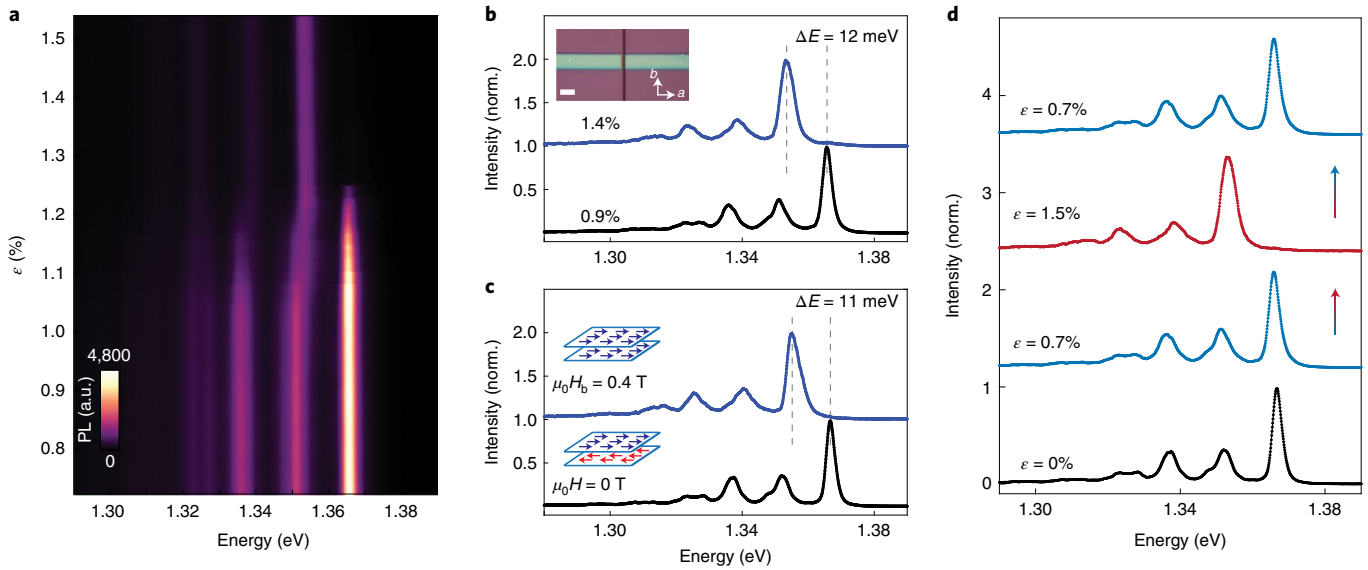

Fig. 2 | Reversible strain-induced AFM-to-FM phase transition. a, Strain-dependent PL intensity plot of a 20 nm CrSBr flake with the strain applied along the *a* axis. The strain is swept up from a starting value of ~0.7%. **b**, PL spectra at 0.9% (black) and 1.4% strain (blue). Inset, optical micrograph of the sample. Scale bar, 30 μm. **c**, PL spectra at a magnetic field of 0 T (black) and 0.4 T applied along the *b* (easy) axis. Insets depict the zero-field A-type AFM and high-field FM states. **d**, Select PL spectra as the strain is swept up and then down. The arrows indicate the progression of applied strain: the strain is ramped up from 0.7% (bottom) to 1.5% (middle) and then back down to 0.7% (top). All the PL spectra are normalized to their maxima and offset for clarity.

bottom inset), all the spins are aligned, resulting in a field-induced FM state (Fig. 2c, top inset). There is an abrupt redshift of about 11 meV in the spectra between the AFM and FM states, whereas the PL pattern remains the same. These magnetic state-dependent PL spectra are remarkably similar to the strain-dependent exciton PL spectra. The slight discrepancy (~1 meV) in the energy difference between the AFM and FM spectra arises from a small additional redshift of the 1.4% high-strain spectra. This comparison thus shows that a strain-induced AFM-to-FM phase transition, with the spins aligned along the easy *b* axis, is responsible for the abrupt change in the PL spectrum.

The strain-induced phase transition is reversible and repeatable. Figure 2d illustrates the PL spectra at selected strains as the strain is continuously swept up and then back down. The black curve at the bottom is taken at a spot far away from the gap, corresponding to zero strain. As the strain increases to the intermediate regime (for example, 0.7%), the spectrum barely changes, consistent with the minor redshift observed in Fig. 2a. At 1.5%, the PL redshifts by ~12 meV, corresponding to the strain-induced FM state. As the strain sweeps back down to 0.7% (Fig. 2d, top blue curve), the exciton PL shifts back to the spectrum corresponding to the AFM state. We note that there is hysteresis between the strain-sweeping directions around the critical strain for the magnetic phase transition (Extended Data Fig. 6).

To further investigate the strain-induced switching of the PL spectrum, we compare the magnetic field response of the strained and unstrained areas of the sample. Figure 3a shows the magneto-PL measurements of the unstrained region with the field applied along the easy axis (*b* axis). The PL is invariant until a critical field $H_c \approx 0.22$ T is reached, at which point the sample undergoes a spin-flip transition to the field-induced FM state (Fig. 3a, insets, show the corresponding magnetic states). On the other hand, when the field is along the *a* axis (Fig. 3b), a continuous redshift of all the main exciton lines is observed as the spins within each layer cant until they eventually align at the saturating field $H_s \approx 0.68$ T. Regardless of the direction of the applied field, the PL spectrum remains invariant when the magnetic field is increased above the saturating field. Similar canting effects are observed for a magnetic field applied along the hard (*c*) axis with a saturating field of $H_s = 1.6$ T (Extended Data Fig. 7). The observed field dependence is consistent with the reported magneto-PL measurements on atomically thin CrSBr samples[24].

In the high-strain state, the sample has a completely different field dependence. Figure 3c shows the magneto-PL measurements with the field applied along the *b* axis of the CrSBr flake at 1.7% strain. In stark contrast to the unstrained case, no detectable difference is observed between the spectra for the high positive field and zero field (Extended Data Fig. 8). As the magnetic field sweeps from positive to negative, the PL remains invariant except at the coercive field near −0.09 T, which corresponds to the switching of the FM states with the spins pointing in opposite directions along the *b* axis (inset in Fig. 3c). This coercive field is more than two times smaller than the one corresponding to the AFM-to-FM transition at zero strain, providing additional evidence that the interlayer magnetic coupling is substantially modified by strain.

For a small range of applied fields near the coercive field (about −0.09 T), the PL intensity suddenly increases, and an additional high-energy peak appears. This observation implies the formation of vertical domains near the switching of the magnetic state, which leads to AF interfaces and thus large PL intensity and additional high-energy peaks. The change in the PL spectrum at the coercive field is hysteretic when the magnetic field is swept up and down (Extended Data Fig. 8). As the field is further increased, the spin orientation of the FM state is fully switched, and the PL goes back to being indistinguishable from the spectra at other magnetic fields. Applying fields along the other axes reveals further differences from the unstrained sample. For instance, no detectable shift is observed in the main exciton lines when the field is swept along the *a* axis (Fig. 3d).

In thin CrSBr samples, the main effect of an applied magnetic field on the exciton PL originates from a dependence of the interlayer electronic hybridization on the interlayer magnetic coupling: the angle between spins in the different layers controls the degree to which the wavefunctions between adjacent layers hybridize[24].

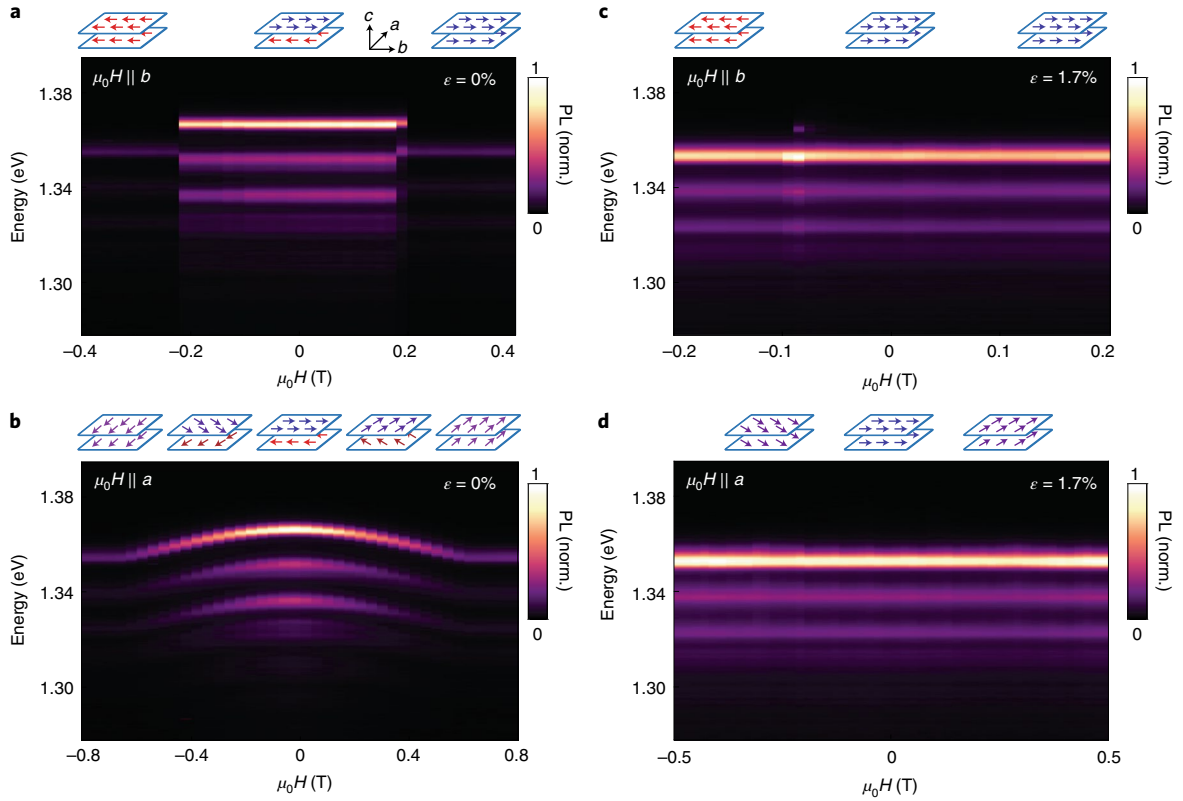

Fig. 3 | Magnetic-field-dependent PL before and after the strain-induced magnetic phase transition. a,**b**, Magnetic-field-dependent PL measurements of unstrained CrSBr with the field applied along the easy (*b*) axis (**a**) and intermediate hard (*a*) axis (**b**). Diagrams over each panel depict the evolution of the magnetic states. **c**,**d**, Magneto-PL measurements along the *b* axis (**c**) and *a* axis (**d**) with a strain of 1.7% applied. Schematic of the FM interlayer magnetic coupling is shown above the intensity plots.

As reported in another study[24], in the AFM state, the anti-aligned spin states in adjacent layers localize the Wannier-type excitons within each layer. As the spins are aligned to the FM state by an applied magnetic field, excitons within each layer delocalize, leading to a redshift in the PL spectrum. In the strain-induced FM phase, the spins would always be aligned except at the coercive field where domains may contain layers with antiparallel orientations, explaining the hysteresis along the easy axis and independence of the PL to fields applied along the intermediate axis. Our analysis is supported by density functional theory (DFT) calculations, which predict a strain-induced AFM-to-FM phase transition (Extended Data Fig. 4b) resulting in a substantial decrease in bandgap, which remains unchanged when the magnetic moment is aligned along the different axes in FM CrSBr (Extended Data Fig. 9). The calculation further shows that the strain-induced magnetic phase transition is not due to a layer stacking rearrangement or changes in interlayer spacing (Extended Data Fig. 4c,d). Rather, it originates from the modulation of the interlayer magnetic exchange interaction by changing the in-plane lattice constant, which affects the geometry of the exchange pathway between Cr atoms in adjacent layers (Extended Data Fig. 10a–c).

Strain tuning of the out-of-plane spin-canting process

We also found that strain leads to dramatic changes in the spin-canting process with an applied out-of-plane magnetic field. Figure 4a shows the normalized polar RMCD, a sensitive probe of the out-of-plane magnetization, at selected strains. At zero strain, the RMCD shows a highly nonlinear dependence on increasing magnetic field, consistent with superconducting quantum interference device measurements on the bulk crystal[26]. This nonlinear behaviour suggests that the out-of-plane spin-canting behaviour in thin bulk CrSBr cannot be explained by a classical Heisenberg model with quadratic anisotropic exchange or single-ion anisotropy, because these terms should yield a linear dependence of magnetization with an out-of-plane magnetic field. Rather, a higher-order magnetic anisotropy term, for example, one originating from biaxial anisotropies, is needed to account for the observation. The application of intermediate strain leads to a large reduction in the saturating magnetic field from 1.6 T (unstrained case) to about 0.9 T (at 1.5% strain). This observation agrees with the DFT calculations, which show that the anisotropic energy (energy difference between the hard- and easy-axis AFM phases) decreases on applying tensile strain along *a* (Extended Data Fig. 10d). Furthermore, as the strain drives the AFM-to-FM phase transition, the RMCD switches from a nonlinear behaviour to linear spin canting, implying strain tuning of high-order magnetic anisotropy. The full strain dependence of RMCD and its derivative with respect to the applied magnetic field are presented as colour plots in Fig. 4b,c, respectively. In the intermediate-strain case, the maximum of the derivative occurs right near the saturating field due to nonlinear spin canting. This saturating field decreases with increasing tensile strain. When the system undergoes the AFM-to-FM phase transition, the derivative becomes constant, indicating the linearity of the RMCD curve. These results demonstrate that both saturating field and spin-canting process can be controlled through strain.

Conclusions

In summary, we have presented new techniques for exploring the effects of uniaxial strain in 2D materials and heterostructures at cryogenic temperatures with in situ tunability. Using these

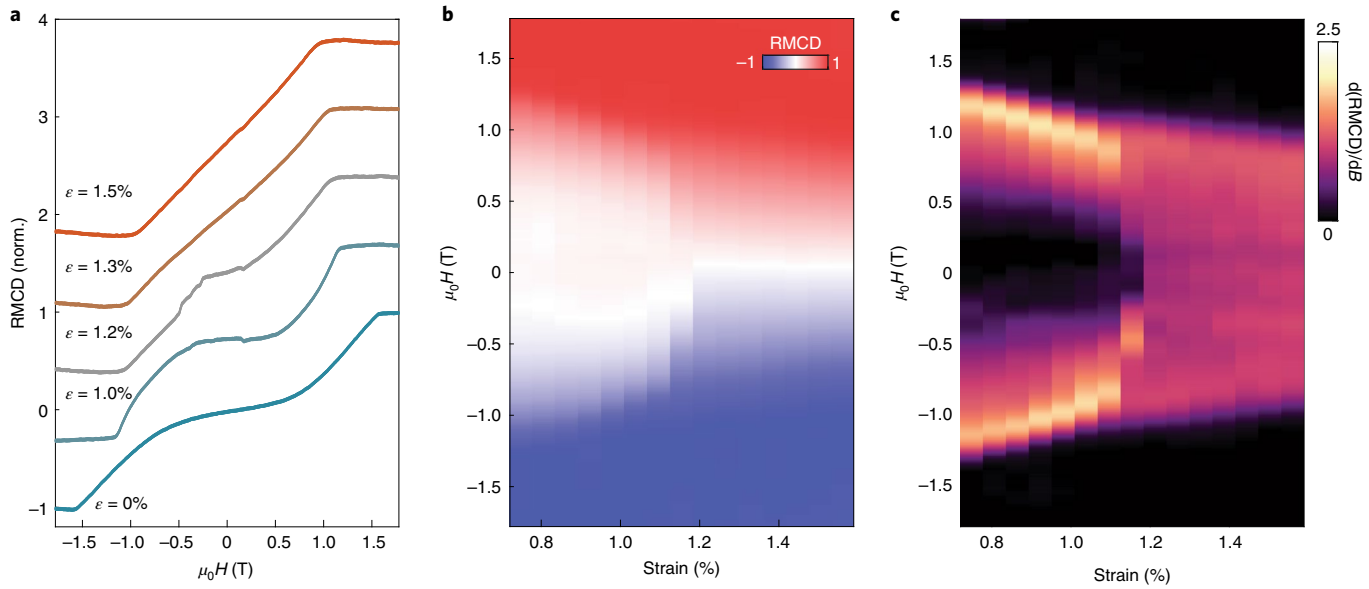

Fig. 4 | Strain tuning of the out-of-plane spin-canting process. a, Polar RMCD measurements as the out-of-plane magnetic field is swept down at select strains. RMCD sweeps are normalized at each strain value. Discrete jumps in the RMCD versus magnetic field near the critical strain (1.2% curve) imply domain effects. **b**, Colour plot of the RMCD sweeps as a function of the applied strain. **c**, Derivative of the normalized RMCD with respect to the applied magnetic field *B* as a function of strain.

techniques, we demonstrate unprecedented control over the magnetic properties of the layered magnetic semiconductor CrSBr. Our results could enable new 2D devices that leverage the unique coupling of spin, charge and lattice, such as strain-actuated magnetoresistive switches, strain tuning of second-harmonic generation via control of magnetic-state-induced inversion symmetry breaking or magnetic tunnel junctions that operate without an applied magnetic field. In addition, strain gradients are inevitable in these devices, for example, near the edge of the gap, which may introduce rich spin textures and open a new path for generating continuously tunable pseudo-magnetic fields[28,29]. Beyond vdW magnets, we envision that these strain platforms can be used to realize dynamic control of structural, electronic and optical properties in many other 2D materials[30–33], heterostructures and moiré superlattices[34].

Online content

Any methods, additional references, Nature Research reporting summaries, source data, extended data, supplementary information, acknowledgements, peer review information; details of author contributions and competing interests; and statements of data and code availability are available at https://doi.org/10.1038/s41565-021-01052-6.

Received: 3 June 2021; Accepted: 16 November 2021;
Published online: 20 January 2022

References

1. Song, T. et al. Giant tunneling magnetoresistance in spin-filter van der Waals heterostructures. *Science* **360**, 1214–1218 (2018).
2. Klein, D. R. et al. Probing magnetism in 2D van der Waals crystalline insulators via electron tunneling. *Science* **360**, 1218–1222 (2018).
3. Wang, Z. et al. Very large tunneling magnetoresistance in layered magnetic semiconductor CrI_3. *Nat. Commun.* **9**, 2516 (2018).
4. Kim, H. H. et al. One million percent tunnel magnetoresistance in a magnetic van der Waals heterostructure. *Nano Lett.* **18**, 4885–4890 (2018).
5. Burch, K. S., Mandrus, D. & Park, J.-G. Magnetism in two-dimensional van der Waals materials. *Nature* **563**, 47–52 (2018).
6. Mak, K. F., Shan, J. & Ralph, D. C. Probing and controlling magnetic states in 2D layered magnetic materials. *Nat. Rev. Phys.* **1**, 646–661 (2019).
7. Li, T. et al. Pressure-controlled interlayer magnetism in atomically thin CrI_3. *Nat. Mater.* **18**, 1303–1308 (2019).
8. Song, T. et al. Switching 2D magnetic states via pressure tuning of layer stacking. *Nat. Mater.* **18**, 1298–1302 (2019).
9. Chu, J.-H. et al. In-plane resistivity anisotropy in an underdoped iron arsenide superconductor. *Science* **329**, 824–826 (2010).
10. Hicks, C. W. et al. Strong increase of T_c of Sr_2RuO_4 under both tensile and compressive strain. *Science* **344**, 283–285 (2014).
11. Chu, J.-H., Kuo, H.-H., Analytis, J. G. & Fisher, I. R. Divergent nematic susceptibility in an iron arsenide superconductor. *Science* **337**, 710–712 (2012).
12. Mutch, J. et al. Evidence for a strain-tuned topological phase transition in $ZrTe_5$. *Sci. Adv.* **5**, eaav9771 (2019).
13. Ceballos, A. et al. Effect of strain and thickness on the transition temperature of epitaxial FeRh thin-films. *Appl. Phys. Lett.* **111**, 172401 (2017).
14. Haskel, D. et al. Pressure tuning of the spin-orbit coupled ground state in Sr_2IrO_4. *Phys. Rev. Lett.* **109**, 027204 (2012).
15. Hong, S. S. et al. Extreme tensile strain states in $La_{0.7}Ca_{0.3}MnO_3$ membranes. *Science* **368**, 71–76 (2020).
16. Šiškins, M. et al. Magnetic and electronic phase transitions probed by nanomechanical resonators. *Nat. Commun.* **11**, 2698 (2020).
17. Wang, Y. et al. Strain-sensitive magnetization reversal of a van der Waals magnet. *Adv. Mater.* **32**, 2004533 (2020).
18. Ni, Z. et al. Imaging the Néel vector switching in the monolayer antiferromagnet $MnPSe_3$ with strain-controlled Ising order. *Nat. Nanotechnol.* **16**, 782–787 (2021).
19. Pizzochero, M. & Yazyev, O. V. Inducing magnetic phase transitions in monolayer CrI_3 via lattice deformations. *J. Phys. Chem. C* **124**, 7585–7590 (2020).
20. Wu, Z., Yu, J. & Yuan, S. Strain-tunable magnetic and electronic properties of monolayer CrI_3. *Phys. Chem. Chem. Phys.* **21**, 7750–7755 (2019).
21. Zhang, J.-M., Nie, Y.-Z., Wang, X.-G., Xia, Q.-L. & Guo, G.-H. Strain modulation of magnetic properties of monolayer and bilayer $FePS_3$ antiferromagnet. *J. Magn. Magn. Mater.* **525**, 167687 (2021).
22. Xu, B. et al. Switching of the magnetic anisotropy via strain in two dimensional multiferroic materials: CrSX (X = Cl, Br, I). *Appl. Phys. Lett.* **116**, 052403 (2020).
23. Hicks, C. W., Barber, M. E., Edkins, S. D., Brodsky, D. O. & Mackenzie, A. P. Piezoelectric-based apparatus for strain tuning. *Rev. Sci. Instrum.* **85**, 065003 (2014).
24. Wilson, N. P. et al. Interlayer electronic coupling on demand in a 2D magnetic semiconductor. *Nat. Mater.* **20**, 1657–1662 (2021).
25. Lee, K. et al. Magnetic order and symmetry in the 2D semiconductor CrSBr. *Nano Lett.* **21**, 3511–3517 (2020).
26. Telford, E. J. et al. Layered antiferromagnetism induces large negative magnetoresistance in the van der Waals semiconductor CrSBr. *Adv. Mater.* **32**, 2003240 (2020).

27. Wang, L. et al. In situ strain tuning in hBN-encapsulated graphene electronic devices. *Nano Lett.* **19**, 4097–4102 (2019).
28. Levy, N. et al. Strain-induced pseudo-magnetic fields greater than 300 Tesla in graphene nanobubbles. *Science* **329**, 544–547 (2010).
29. Mao, J. et al. Evidence of flat bands and correlated states in buckled graphene superlattices. *Nature* **584**, 215–220 (2020).
30. Pető, J. et al. Moderate strain induced indirect bandgap and conduction electrons in MoS_2 single layers. *npj 2D Mater. Appl.* **3**, 39 (2019).
31. Conley, H. J. et al. Bandgap engineering of strained monolayer and bilayer MoS_2. *Nano Lett.* **13**, 3626–3630 (2013).
32. He, K., Poole, C., Mak, K. F. & Shan, J. Experimental demonstration of continuous electronic structure tuning via strain in atomically thin MoS_2. *Nano Lett.* **13**, 2931–2936 (2013).
33. Lee, J., Wang, Z., Xie, H., Mak, K. F. & Shan, J. Valley magnetoelectricity in single-layer MoS_2. *Nat. Mater.* **16**, 887–891 (2017).
34. Andrei, E. Y. et al. The marvels of moiré materials. *Nat. Rev. Mater.* **6**, 201–206 (2021).

Methods

Strain cell. To apply strain to the samples, we constructed home-built strain cells consisting of three piezoelectric actuators glued in parallel to a titanium backing plate and a titanium flexure element. The flexure element consists of a W-shaped outer piece and a rectangular inner block, with a 0.5 mm gap formed between them (Fig. 1a). The outer and inner piezo stacks are oppositely poled; applying a positive voltage causes the outer piezo stacks to expand and the inner one to contract, thereby opening the gap. This configuration also minimizes the built-in thermal strain, as the two sides of the gap move together when cooled. The measurements shown in Fig. 1d and Extended Data Fig. 5 were taken using a CS100 strain cell (Razorbill Instruments), which uses a similar operating principle.

Sample preparation and strain gauge calibration. In our experiments, pieces of 285 nm SiO_2/Si substrate were adhered onto 2D flexure sample plates produced by Razorbill Instruments using STYCAST 2850FT epoxy. To reduce the effective spring constant of strained silicon, we chose thin (50 µm) silicon wafers and cut them into narrow (~300 µm) pillars. The distance between the epoxied ends is ~400 µm, giving an effective spring constant of $k = Y\frac{A}{L} \approx 5\frac{N}{\mu m}$, where we use a value of 130 GPa for the Young's modulus of silicon[35]. This value is much lower than the blocking force of the piezo stacks, enabling the application of strain. To calibrate the strain applied to the silicon pillar, we used the shift rate reported in ref. [36].

After the pillar was glued in place, we transferred the strain gauge heterostructure on top of it via a dry transfer technique using a stamp consisting of a polypropylene carbonate film spin coated on top of a polydimethylsiloxane cylinder. Flakes were picked up in the following order: 20–30 nm top hexagonal boron nitride, graphene and >20 nm CrSBr. The pillar was then aligned with the long axis of the CrSBr flake, which is the crystal *a* axis, and then the stack was deposited on top of it. The strain applied to graphene was determined by the same shift rate used in ref. [27], which comes from ab initio calculations[37]. Bulk single-crystal CrSBr was synthesized using the same method detailed in other works[24–26].

For suspended samples, large rectangular pieces of the same substrate were glued to the titanium sample plate and then fractured with a diamond scribe. The fracture produces a gap of ~3–5 µm, with nearly uniform height on both sides. The sample plate is then screwed to the strainer, and the thin CrSBr is transferred over the gap using the same dry transfer method. The entire strain apparatus is then loaded into the cryostat for measurement.

Optical measurements. Optical measurements of the strain gauge heterostructure were performed using backscattering geometry in a closed-cycle helium cryostat (OptiCool by Quantum Design) with a nominal sample temperature of 2.2 K. An objective lens focused 632.8 nm light from a He/Ne laser to a spot size of ~1 µm. The collected signal was dispersed using a grating with a groove density of 1,200 mm^{-1} and detected with a liquid-nitrogen-cooled charge-coupled device. A laser power of 300 µW was used for the Raman measurements, with integration times of 120 s for graphene and 30 s for both CrSBr and silicon spectra. BragGrate notch filters were utilized to reject Rayleigh scattering down to 5 cm^{-1}. Measurements of the suspended sample (Fig. 1d and Extended Data Fig. 5) were taken in a cold-finger cryostat from Montana Instruments at a sample temperature of ~15 K. All the other data from the suspended samples were taken using a vector magnet cryostat from Montana Instruments at a nominal sample temperature of about 5 K. For the PL measurements, we used 4 µW of power and the collected light was dispersed by a grating with a groove density of 600 mm^{-1}. To increase the spatial sensitivity of the experiment, a confocal setup with 50 µm pinhole was used. The RMCD measurements were taken using the same setup previously used to study CrI_3 (ref. [38]).

Finite-element analysis. We used the ANSYS Mechanical 2021 R1 finite-element analysis software to calculate and visualize the strain distribution on the top surface of a strained silicon pillar. The model geometry and dimensions match our experimental conditions: the pillar is 50 µm thick, 1 mm long and 300 µm wide. A 285 nm layer of SiO_2 is placed on top of the silicon; underneath, there are two 10-µm-thick pads of STYCAST 2850FT epoxy that form a 400 µm gap. The contact between the materials is modelled via a shared topology between each solid. The boundary conditions are set to apply a 5 µm displacement to the bottom face of each epoxy pad directed parallel to the pillar's long axis. We use the elastic constants reported in ref. [35] for the <110> directions of a (100) wafer. To account for the orthotropic elasticity in silicon, we made an additional model that was rotated by 45° such that strain is applied along the [100] axis. In both cases, the total strain variation across the middle of the pillar was less than 0.01%. The SiO_2 layer is modelled with isotropic elasticity with a Young's modulus of 70 GPa and Poisson's ratio of 0.17, whereas the STYCAST epoxy was modelled using elastic constants provided in ref. [23].

First-principles calculations. First-principles calculations of few-layer and bulk CrSBr were performed using DFT implemented in the QUANTUM ESPRESSO package[39]. We employed norm-conserving pseudopotentials[40], with a plane-wave energy cutoff of 85 Ry. In structural relaxation, we used the spin-polarized Perdew–Burke–Ernzerhof exchange–correlation functional that included dispersion corrections within the D2 formalism[41] to account for the vdW interactions. The structure was fully relaxed until the force on each atom was smaller than 0.002 eV $Å^{-1}$. The calculated equilibrium lattice constants along the *a* and *b* axes were 3.5 and 4.7 Å, respectively. The calculated interlayer distance was 8.0 Å in the bulk. These results were in excellent agreement with the experiments[26], showing errors of <1%. The applied strain along the intermediate axis was calculated in percentile relative to the equilibrium structure. For each strain, the energy differences between the interlayer AFM and FM phases were calculated within the local spin density approximation. We note that the calculated value of critical strain can be affected by factors such as the choice of pseudopotential used in the calculations. We find that an on-site Hubbard *U* correction is not needed to reproduce the correct magnetic ground-state properties of bulk CrSBr. The calculation of the Raman-active phonon modes used the frozen-phonon method.

Data availability

Source data are provided with this paper. All other data that support the findings of this study are available from the corresponding authors upon reasonable request.

References

35. Hopcroft, M. A., Nix, W. D. & Kenny, T. W. What is the Young's modulus of silicon? *J. Microelectromech. Syst.* **19**, 229–238 (2010).
36. Ureña, F., Olsen, S. H. & Raskin, J.-P. Raman measurements of uniaxial strain in silicon nanostructures. *J. Appl. Phys.* **114**, 144507 (2013).
37. Mohr, M., Papagelis, K., Maultzsch, J. & Thomsen, C. Two-dimensional electronic and vibrational band structure of uniaxially strained graphene from ab initio calculations. *Phys. Rev. B* **80**, 205410 (2009).
38. Huang, B. et al. Layer-dependent ferromagnetism in a van der Waals crystal down to the monolayer limit. *Nature* **546**, 270–273 (2017).
39. Giannozzi, P. et al. QUANTUM ESPRESSO: a modular and open-source software project for quantum simulations of materials. *J. Phys. Condens. Matter* **21**, 395502 (2009).
40. Hamann, D. R. Optimized norm-conserving Vanderbilt pseudopotentials. *Phys. Rev. B* **88**, 085117 (2013).
41. Grimme, S. Semiempirical GGA-type density functional constructed with a long-range dispersion correction. *J. Comput. Chem.* **27**, 1787–1799 (2006).

Acknowledgements

We thank K. Seyler, D. Cobden and M. Yankowitz for their helpful discussions on the strain devices. The strain-induced magnetic phase transition project is mainly supported by the US Department of Energy (DOE), Basic Energy Sciences (BES), under award DE-SC0018171. Part of the strain setup and RMCD measurements are supported by the Air Force Office of Scientific Research (AFOSR) Multidisciplinary University Research Initiative (MURI) program via grant no. FA9550-19-1-0390 and the Gordon and Betty Moore Foundation's EPiQS Initiative via grant GBMF6759 to J.-H.C. The first-principles calculation is mainly supported by NSF MRSEC DMR-1719797. K.X. acknowledges the Graduate Fellowship from Clean Energy Institute funded by the State of Washington. Z.L. and J.-H.C. acknowledge the support of the David and Lucile Packard Foundation. T.C. acknowledges support from the Micron Foundation. Computational resources were provided by HYAK at the University of Washington. CrSBr crystal synthesis is supported by the Center on Programmable Quantum Materials, an Energy Frontier Research Center funded by the US DOE, Office of Science, BES, under award DESC0019443.

Author contributions

X.X. and J.C. conceived the experiment. J.C. designed and built the strain cell, with assistance from Z.L., and J.-H.C., E.A. and J.F. helped with the integration of the strain apparatus to cryostats. J.C. fabricated the samples and performed the optical measurements with help from P.T., and A.M., J.C., S.S., X.X., T.C., D.X. and J.-H.C. interpreted the results. A.D. grew and characterized the bulk CrSBr crystals with supervision from X.R., and X.Z., S.S., K.X. and T.C. provided the first-principles calculations with input from D.X. A.M. performed the finite-element analysis modelling with guidance from J.C. J.C., X.X. and T.C. wrote the manuscript in consultation with all the authors. All the authors discussed the results.

Competing interests

The authors declare no competing interests.

Additional information

Extended data is available for this paper at https://doi.org/10.1038/s41565-021-01052-6.

Supplementary information The online version contains supplementary material available at https://doi.org/10.1038/s41565-021-01052-6.

Correspondence and requests for materials should be addressed to Ting Cao or Xiaodong Xu.

Peer review information *Nature Nanotechnology* thanks Wei Ji, Liang Wu and the other, anonymous, reviewer(s) for their contribution to the peer review of this work.

Reprints and permissions information is available at www.nature.com/reprints.

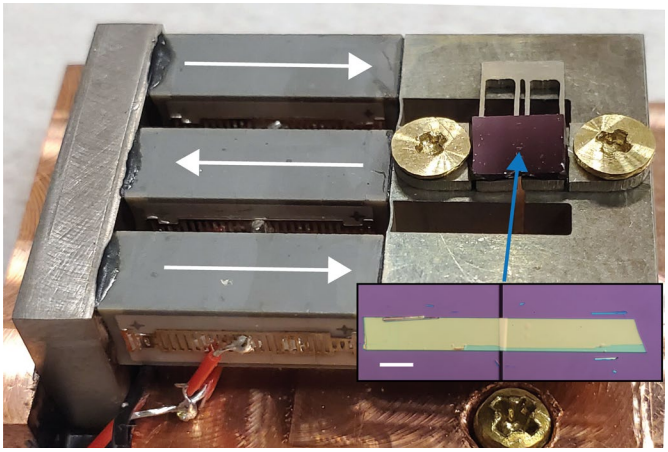

Extended Data Fig. 1 | Photograph of strain cell and mounted CrSBr flake. The strain cell consists of three piezoelectric actuators glued to a titanium flexure element. The white arrows indicate the direction of motion when a positive voltage is applied. Inset, optical micrograph showing a zoom-in on the CrSBr flake, which is indicated by the blue arrow. Scale bar: 30 μm.

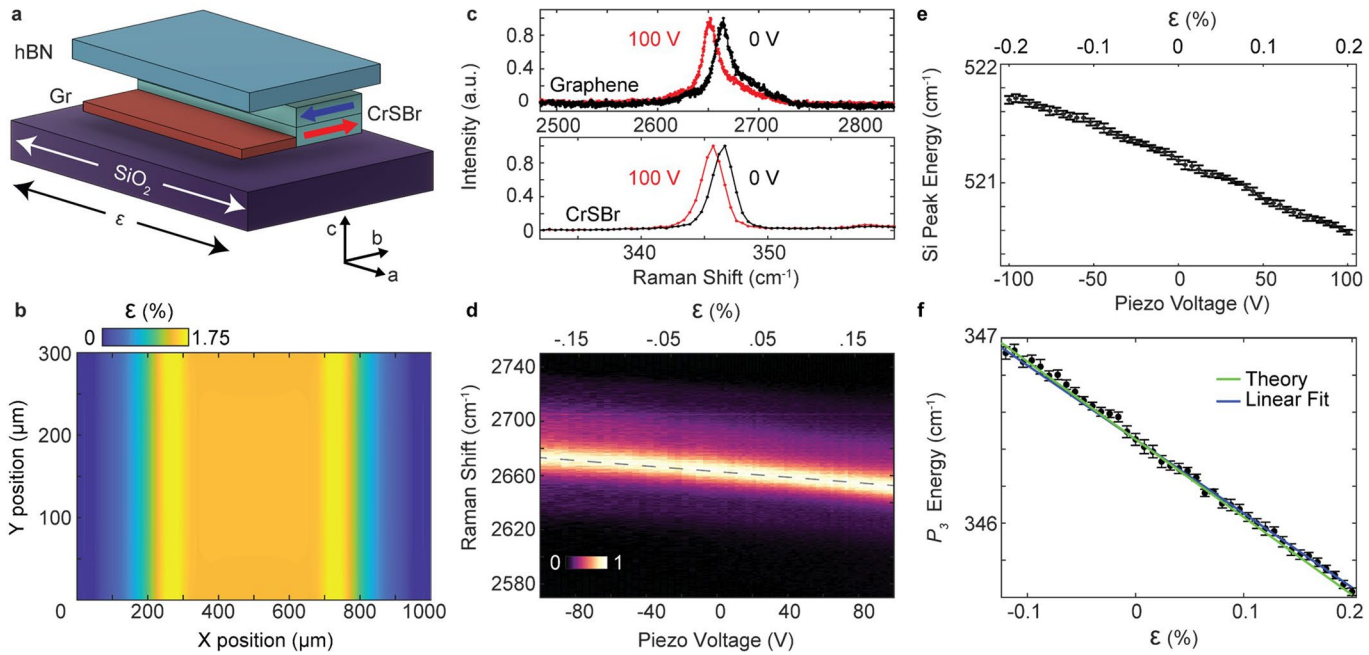

Extended Data Fig. 2 | Calibration of CrSBr strain response using a strain gauge heterostructure. a, Diagram of a hBN/CrSBr/graphene strain gauge heterostructure deposited on a Si/SiO_2 pillar. When the pillar is strained, the strain is transferred to the heterostructure on top. In our experiments, the strain is aligned with the *a* crystal axis of the CrSBr, which is the magnetic intermediate axis orthogonal to the easy (*b*) axis. The red and blue arrows on the CrSBr depict the AFM interlayer coupling which produces an A-type layered AFM structure. **b**, Finite element analysis modelling using parameters similar to those of our experiment (see Methods). The modelling shows that the surface of the pillar has a highly uniform strain profile (< 0.01% total variation) over the length scale of the sample across the middle of the pillar. **c**, Raman spectra of the graphene 2D peak (top) and CrSBr Raman mode centered around 346 cm^{-1} (bottom) with 0 (black) and 100 (red) volts applied to the strain cell. **d**, Full strain dependence of the graphene 2D peak. The grey line represents a linear fit of the peak position as a function of piezo voltage determined by Lorentzian fits. The strain values are then calculated using a previously reported[28,38] Raman shift rate of graphene. **e**, Energy of the silicon Raman peak as a function of piezo voltage. Using the previously reported[37] strain shift rate yields a calibration which is essentially the same as that determined from the graphene spectra. In order to determine the amount of built-in strain due to preparation of the silicon substrate and differences in thermal expansion coefficients, we also measured a freestanding silicon chip glued next to the strained chip. Comparing the strained silicon pillar at zero volts to the freestanding chip right next to it, we found that the built-in strain on this particular pillar was negligible. **f**, CrSBr Raman peak extracted from Lorentzian fits as a function of strain along with linear fits to the data (blue line) and the first-principles calculated Raman shift rate (green line, shifted vertically to ~ 346 cm^{-1} at V = 0). Error bars in **e-f** represent the uncertainty of the Lorentzian fits.

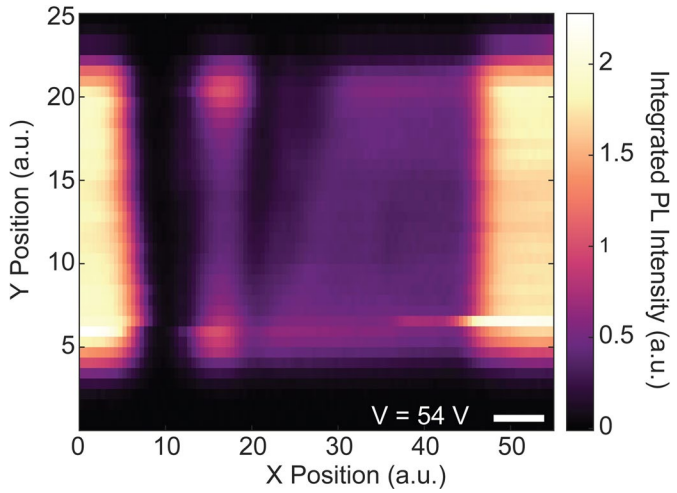

Extended Data Fig. 3 | Photoluminescence (PL) intensity map of sample S2. Spatial map of PL intensity integrated from 1.363 eV to 1.39 eV with 54 V applied to the piezo stacks. This spectral range captures PL from the highest energy exciton in the AFM state, but not in the FM state. That is, the dark regions in the PL map are the most strained, as they are in the FM state, whereas the brightest regions have the strongest AFM state and thus have the lowest strain. Scalebar: 10 μm. The data presented in the paper were taken in the center of the high strain region.

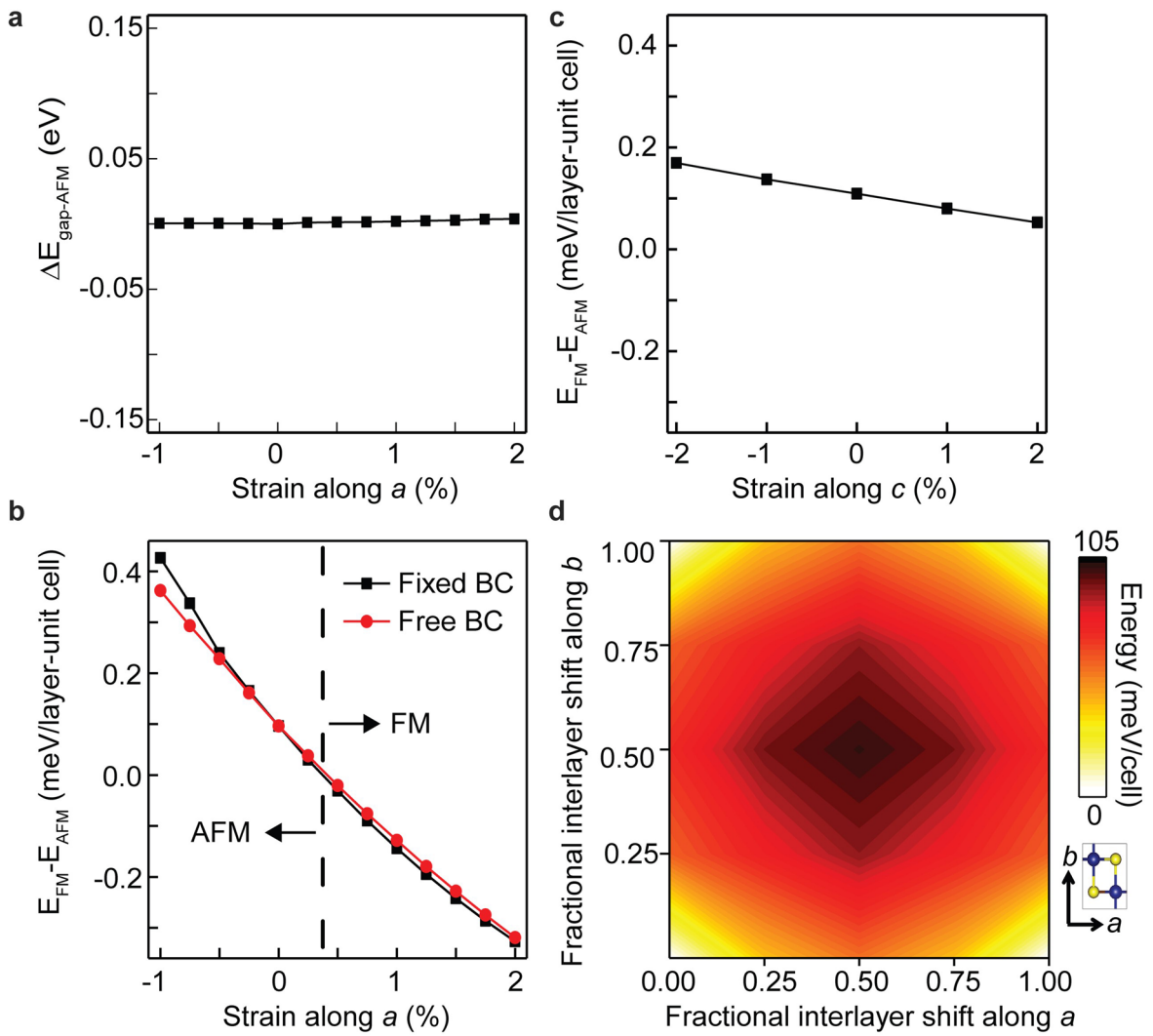

Extended Data Fig. 4 | DFT scalar-relativistic calculations of strain effects on band gap and interlayer magnetic ordering. a, DFT-LSDA calculated change of the band gap, $\Delta E_{gap\text{-}AFM}$, of bulk CrSBr in the interlayer AFM phase as the strain is applied along *a*-axis, while *b*- and *c*-axes are free to relax. $\Delta E_{gap\text{-}AFM}$ is < 5 meV for < ±1% strain. **b**, DFT-LSDA calculation of energy difference Δ between the interlayer FM and AFM states as a function of strain applied along the *a* axis. The sign switching from positive to negative as strain increases indicates a strain-induced AFM to FM transition, denoted by the dashed black line. We found that the calculated Δ shows little difference between fixed- and free-boundary conditions, that is, if the lattice constants in *b* and *c* are kept constant (black) or free to relax (red). In the latter case, the change in lattice constant *b* and *c* are − 0.1% and − 0.4%, respectively, for a 1% strain along *a*, in bulk CrSBr. **c**, DFT-LSDA calculations of the energy difference of FM and AFM interlayer coupling as a function of strain applied along the *c* axis with lattice constants in *a* and *b* kept constant. CrSBr stays in the AFM phase within ± 2% strain. The results in both (**b**) and (**c**) suggest that the sign switching of the interlayer magnetic exchange interaction is not a result of changes to the interlayer spacing caused by the Poisson effect. **d**, Calculated total stacking-dependent energy of AFM bilayer CrSBr. A 4×4 grid is used to sample real-space shift vectors between one layer relative to the other. We find only one stable interlayer stacking configuration at (0, 0). Combined with the experimentally demonstrated reversible tunability, we rule out switching of the lateral layer-stacking arrangement as the cause of AFM-FM phase transition.

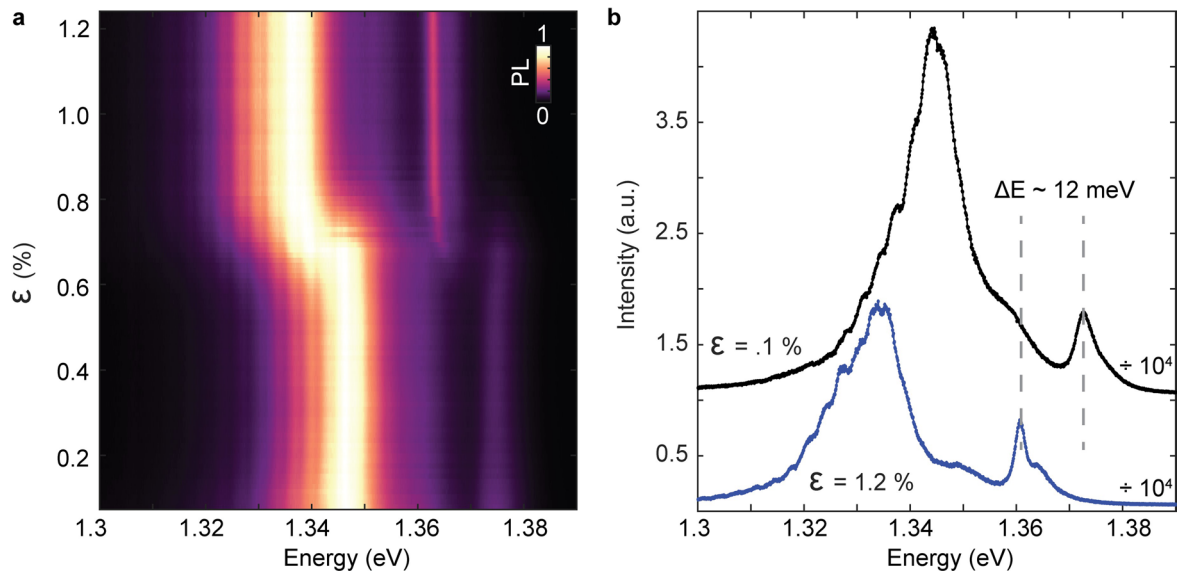

Extended Data Fig. 5 | Strain-induced phase transition in a second suspended sample. a, Strain dependent PL measurements of a second exfoliated CrSBr sample. The spectra are normalized to he maxima at each strain. The nominal sample temperature is 15 K. **b**, PL spectra at strains below (black) and above (blue) the phase transition reveal a ~ 12 meV redshift between the two.

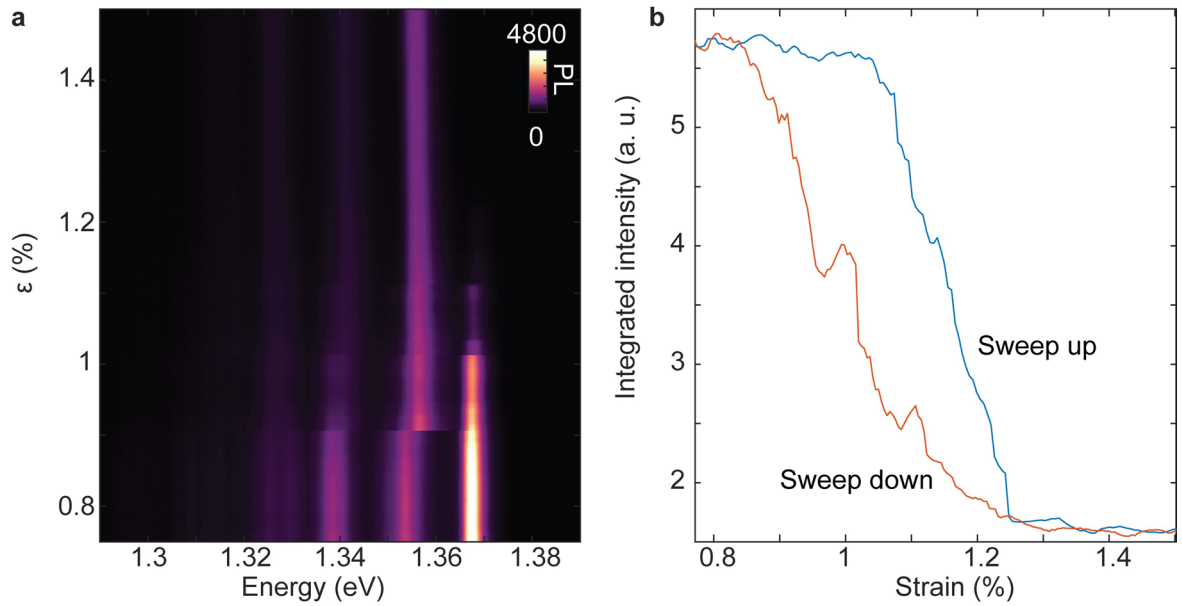

Extended Data Fig. 6 | Hysteresis in the strain-induced magnetic phase transition. a, Intensity plot of PL as a function of strain as the piezo voltage is swept down from a high strain state. **b**, Integrated intensity of the entire spectral range as the strain is swept up (blue) and down (orange). To account for hysteresis in the piezostacks, we calibrated the strain using Raman sweeps in the same direction.

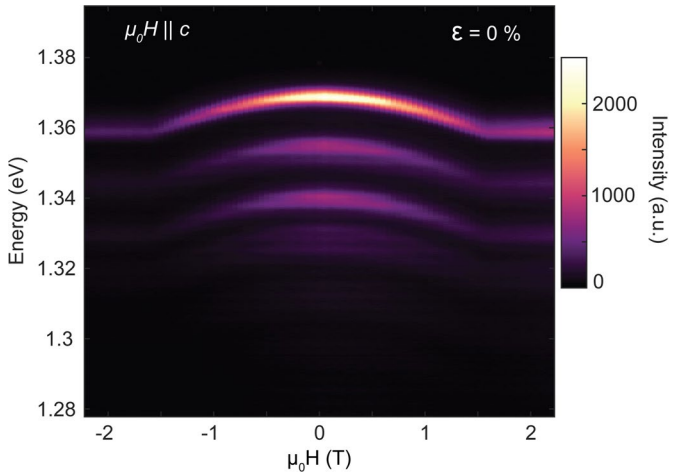

Extended Data Fig. 7 | Magneto-photoluminescence measurements with the field swept along the hard (*c*) axis. Magnetic field dependent PL measurement of unstrained CrSBr as the field is swept along the *c* crystal axis (magnetic hard axis).

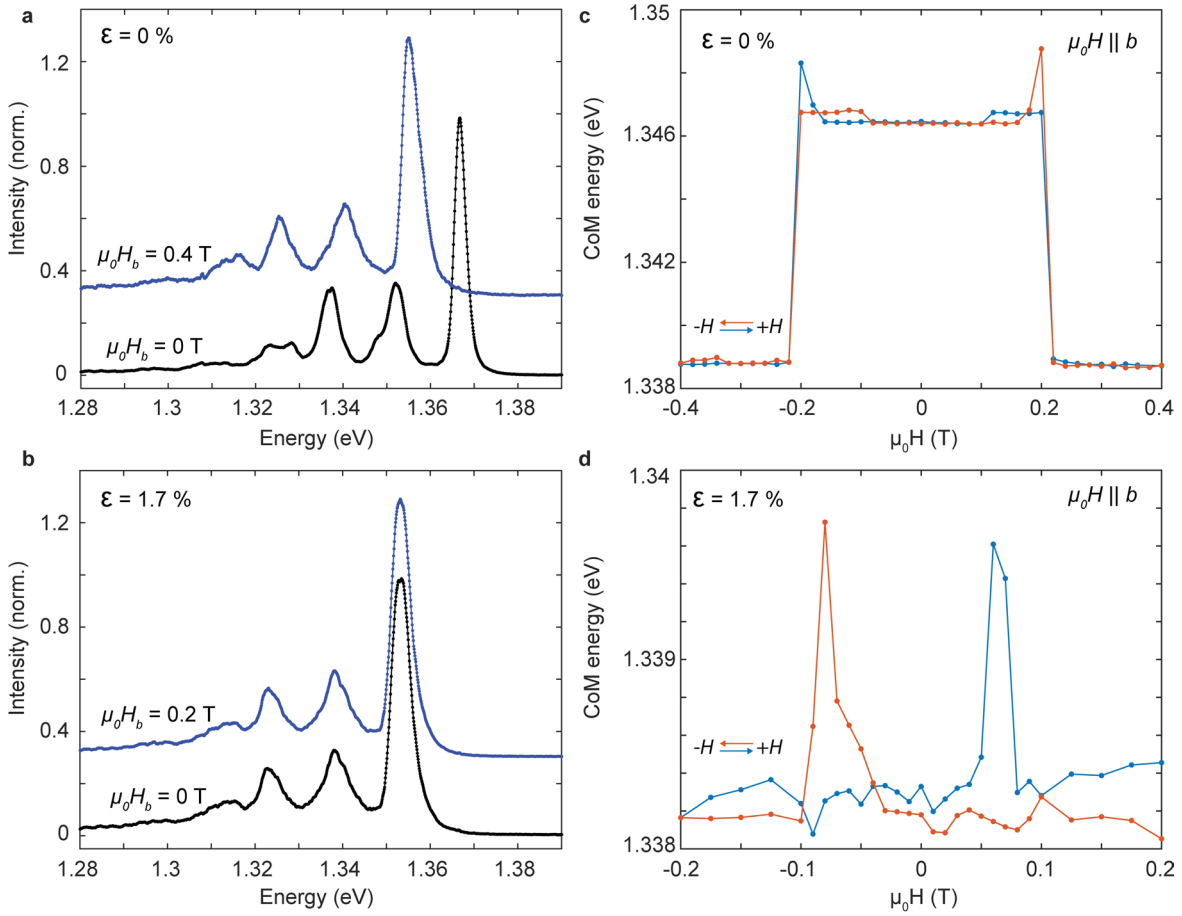

Extended Data Fig. 8 | Comparison of photoluminescence at select magnetic fields and integrated intensity of unstrained and highly strained CrSBr. **a-b**, PL spectrum of unstrained (**a**) and highly strained (**b**) CrSBr at zero (black) and saturating (blue) magnetic field μ_0H applied along the easy *b*-axis. **c-d**, Extracted center of mass (COM) of the entire spectra range as a function of μ_0H || *b*-axis in the unstrained (**c**) and highly strained (**d**) samples.

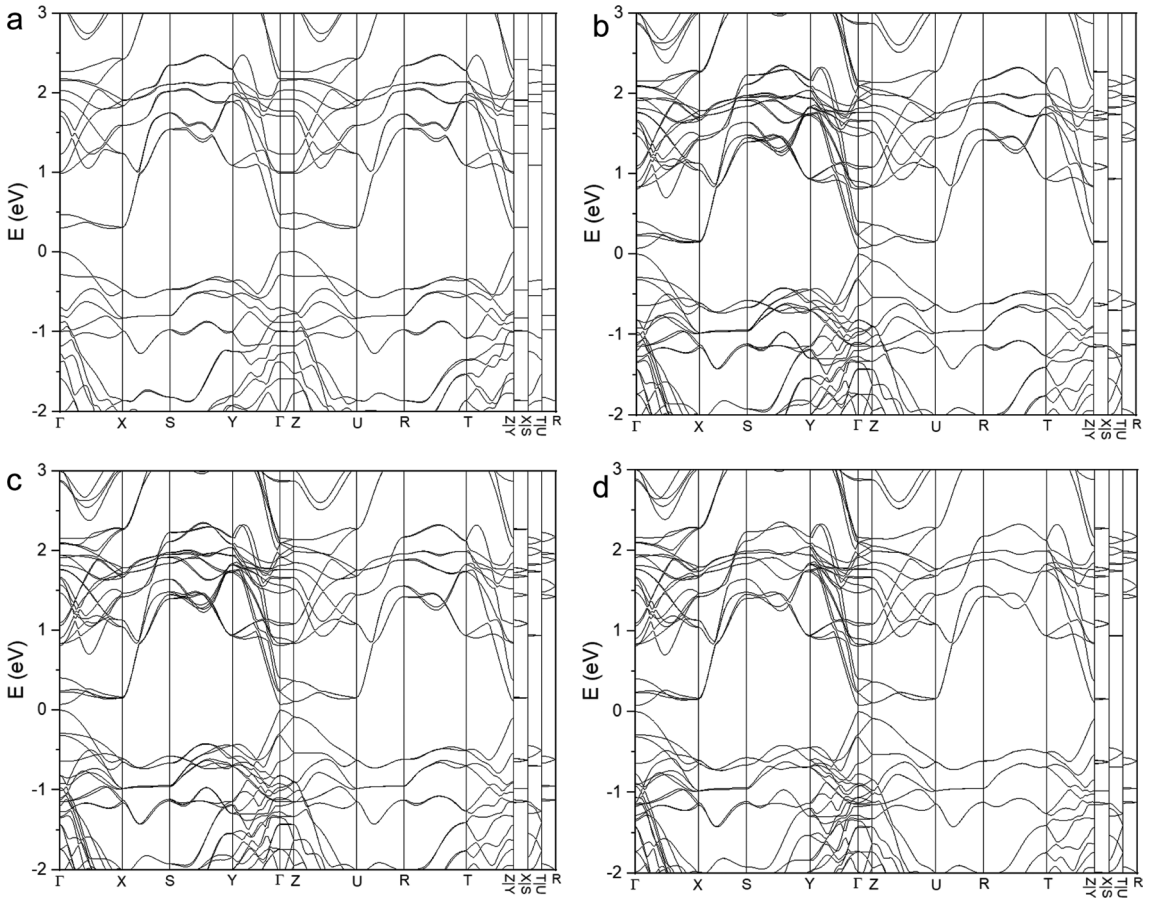

Extended Data Fig. 9 | Fully-relativistic Kohn-Sham DFT band structures of bulk CrSBr with 1.5% uniaxial strain applied along the a axis. a, AFM CrSBr with magnetic moment constrained along the easy *b* axis. **b**, **c**, **d**, FM CrSBr with magnetic moment constrained along the *b*, *a*, and *c* axes, respectively. Due to the stronger interlayer hybridization in the FM phase, the top valence band and bottom conduction band at Gamma split into subband groups, resulting in a smaller Kohn-Sham band gap than that of the AFM phase. Once in the FM phase, the bandgap shows no appreciable difference when the magnetic moment is aligned along the different axes. These features agree well with our strain and magnetic field dependent measurements. We note, however, that Kohn-Sham DFT at the mean-field level has been known to underestimate the band gaps of semiconductors, and the band gaps presented here should not be directly compared to the PL energy levels in the present work. Optimized norm-conserving Vanderbilt pseudopotentials are employed in the fully-relativistic calculations with similar generation parameters to the scalar-relativistic pseudopotentials.

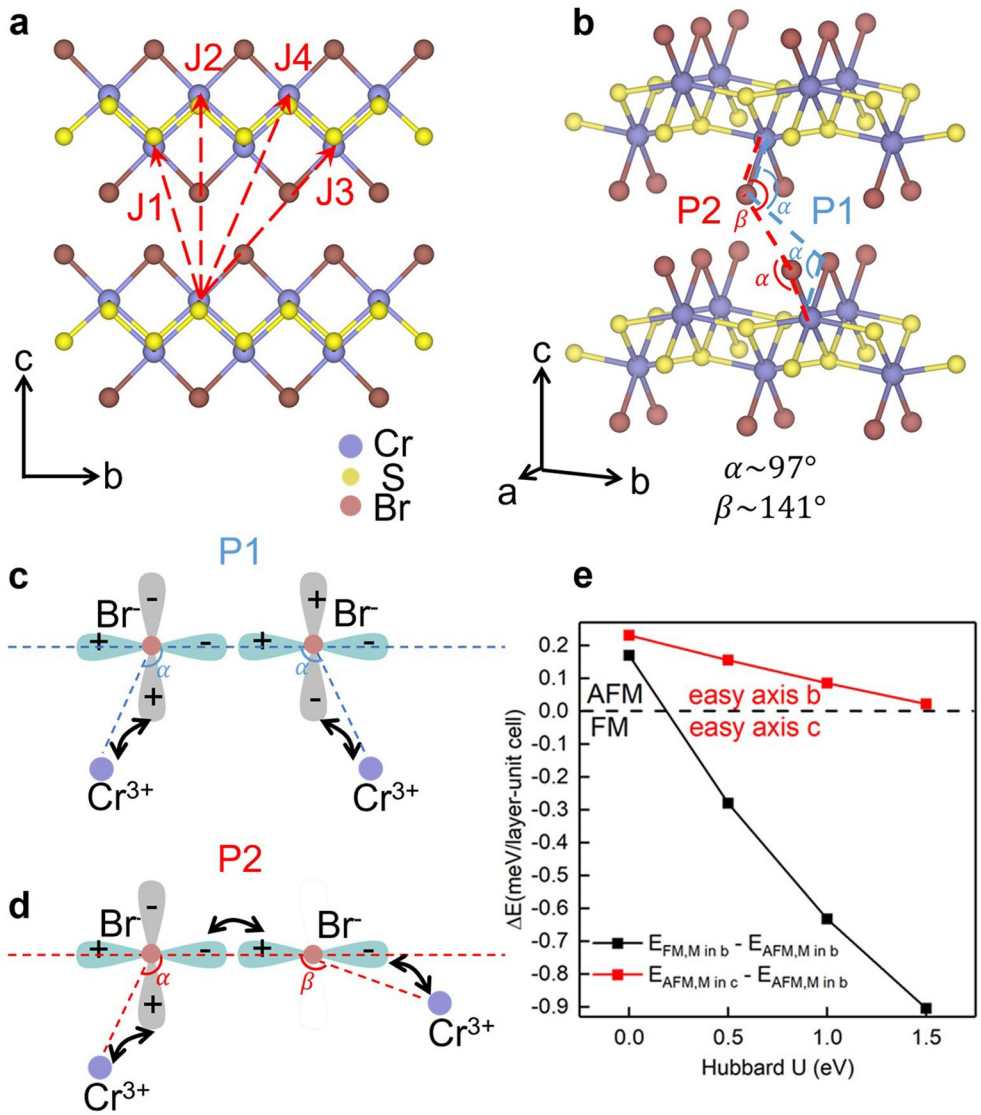

Extended Data Fig. 10 | Effects of strain on exchange pathways and magnetic anisotropic energy in CrSBr. a, The interlayer magnetic exchange coupling J1, J2, J3 and J4 for the 1st, 2nd, 3rd, and 4th nearest-neighbor (NN) interlayer Cr pairs. The strain-induced magnetic phase transition is likely driven by a significant enhancement in the 1st NN interlayer Cr-Cr coupling which favors ferromagnetism. **b**, Two interlayer magnetic exchange pathways between closest Cr-Cr interlayer pairs in side view. **c**, Schematics of the first exchange pathway, giving weaker magnetic exchange coupling. Due to the nearly orthogonal Br p orbitals in the super-super exchange pathway, the magnetic coupling is mediated by the weak on-site interaction between the p orbitals (Hund's rule) in both Br. **d**, Schematics of the second exchange pathway that favors AFM coupling when α goes closer to 180° (compressive strain along *a*), and FM coupling when α approaches 90° (tensile strain along *a*), in agreement with the first principles calculation. Since this pathway allows for direct hopping in one of the Br, it should dominate the interlayer magnetic coupling between closest Cr-Cr interlayer pairs. **e**, Magnetic anisotropic energies as a function of uniaxial strain along *a*, obtained from fully-relativistic calculations, with the free boundary condition. The black and red points correspond, respectively, to the energy difference between the hard- and easy-axis AFM phase, and the energy difference between the hard-axis FM phase and the easy-axis AFM phase. The decreasing anisotropic energies agree with the observed decrease of saturating field in the spin canting process upon straining.